# Propagating characteristics of mesospheric gravity waves observed by an OI 557.7 nm airglow all-sky camera at Mt. Bohyun (36.2°N, 128.9°E)

Jun-Young Hwang[1], Young-Sook Lee[1], Yong Ha Kim[1], Hosik Kam[2], Seok-Min Song[1], Young-Sil Kwak[2,3], Tae-Yong Yang[2]

[1]Department of Astronomy and Space Science, Chungnam National University, 34134, Daejeon, South Korea.
[2]Korea Astronomy and Space Science Institute, Daejeon, 34055, South Korea.

[3]Department of Astronomy and Space Science, University of Science and Technology, Daejeon, 34113, South Korea.

*Correspondence to*: Young-Sook Lee (yslee0923@cnu.ac.kr)

**Abstract.** We analysed all-sky camera images observed at Mt. Bohyun observatory (36.2°N, 128.9°E) for the period of 2017 - 2019. The image data were acquired with a narrow band filter centred at 557.7 nm for the OI airglow emission at ~96 km altitude. The total of 150 wave events were identified in the images of 144 clear nights. The interquartile ranges of wavelength, phase speed, and periods of the identified waves are 20.5 - 35.5 km, 27.4 - 45.0 m/s and 10.8 -13.7 min with the median values of 27.8 km, 36.3 m/s and 11.7 min, respectively. The summer and spring bias of propagation directions of northeast- and northward, respectively, can be interpreted as the effect of filtering by the prevailing winds in the lower atmosphere. In winter the subdominant north-westward waves may be observed due to nullified filtering effect by small northward background wind or secondary waves generated in the upper atmosphere. Intrinsic phase speeds and periods of the waves were also derived by using the wind data simultaneously observed by a nearly co-located meteor radar. The nature of vertical propagation was evaluated in each season. The majority of observed waves are found to be freely propagating, and thus can be attributed to wave sources in the lower or upper atmosphere.

## 1 Introduction

Short-period atmospheric gravity waves (<100 min) are well known for playing an important role in carrying energy and momentum from the lower atmosphere, upward propagating and depositing them into the mesosphere and lower thermosphere (MLT) region (Lindzen, 1981; Fritts and Alexander, 2003). In the mid- and high-latitude MLT region the transported energy and momentum are deposited through the breaking and dissipating processes of gravity waves, and affect significantly the zonal flow in both hemispheres, which in turn causes the pole-to-pole circulation resulting in the cold and warm mesosphere in summer and winter, respectively (Lindzen, 1981; Fritts and Vincent, 1987; Fritts and Alexander, 2003; Becker, 2012). Atmospheric gravity waves are generated by a number of causes or mechanisms, such as mountainous terrain,

convective activity triggered by severe weather phenomena, wind shear, and areas with high baroclinic instability (Fritts and Alexander, 2003).

The characteristics of short-period gravity waves have been studied by the observation of airglow emission in the MLT region. Airglow imaging technique has been developed to observe gravity waves directly by using a wide-field or all-sky lens with a highly sensitive cooled charge-coupled device (CCD) detector. The observation using an all-sky camera has an advantage of being able to derive various parameters of gravity waves through series of processing in time and spatial domains. Time series of all-sky airglow images can be converted into series of 2-dimensional image arrays that can be analysed objectively to obtain the horizontal wavelength, propagation phase speed and period of the wave (Taylor et al., 1993).

An all-sky imager had been deployed at Bohyun observatory (BHO, 36.2°N, 128.9° E) to observe various airglows, including OH Meinel 720-910 nm, $O_2$ atmospheric band near 865.7 nm, OI 630 nm and OI 557.7 nm in the pilot period of 2002 - 2005. Later, the all-sky camera at BHO focused on the OI 557.7 airglow observation because the throughput of the OI 557.7 filter is far more efficient than other filters. The previous studies with the all-sky observation at BHO have reported seasonal variation of wave parameters and horizontal propagation directions (Kim et al., 2010; Yang et al., 2015).

The characteristics of vertical propagation of gravity waves can be determined by the relationship between the horizontal phase speed of gravity waves and the background wind field, and vertical temperature profile. The nature of vertical propagation can be classified into critical-level filtering, ducting, and freely propagating modes. Critical-level filtering effect is caused when the horizontally propagating wave meets with the same vector of background wind, and the wave would be absorbed or reflected out (Kim and Chun, 2010; Heale and Snively, 2015). The wave that is reflected from the upper and (or) lower altitude regions can be (partially) ducted (Fritts and Alexander, 2003). The wave ducting can occur when the wave propagates against background wind field, at which background wind profile has a local maximum, called Doppler ducting (Chimonas and Hines, 1986; Isler, 1997; Nappo, 2002; Suzuki et al., 2013). In addition, large vertical changes of background winds such as wind shear or curvature wind can provide a favourable condition to cause Doppler ducting (e.g., Chimonas and Hines,1986; Isler et al., 1997). The ducted wave can horizontally propagate much longer distance than freely propagating waves (Isler et al., 1997; Hecht et al., 2001; Pautet et al., 2005). In freely propagating mode, horizontally propagating waves can be Doppler shifted by opposing or forwarding background wind. Therefore, the background wind can play a crucial role in evaluating the nature of both vertical and horizontal propagation of gravity waves. Fortunately, we were able to take advantage of the background wind measurements around the OI airglow layer by a meteor radar (MR) at Gyeryong nearby BHO.

This study reports the characteristics of the observed and intrinsic parameters of gravity waves by using the all-sky imaging data for the period of 2017 – 2019 along with the mesospheric wind data that were simultaneously observed by a meteor radar. The intrinsic parameters of gravity waves allow to understand the relation between the observed wave directions and the background winds as well as the nature of vertical propagation at mid-latitude mesosphere around the east Asia.

## 2 Observational and model data

We analysed OI 557.7 airglow images observed by the all-sky camera at BHO from April 2017 through December 2019. Images of the total 144 nights were used in the analysis by excluding the cases of cloudy and moon-lit nights and equipment malfunction. The all-sky camera at BHO is an ultra-high speed (f/0.95) 3-inch camera composed of a fisheye lens with a viewing angle of 180°, telecentric lens to adjust airglow emission light path for parallel incident to filter, a 6-position filter wheel installed with two narrowband filters (OI-557.7, OI-630.0), and a 1024×1025 CCD detector. All-sky images were obtained with 4×4 binning to increase signal to noise ratios. The detailed description of the all-sky camera at BHO has been given in Yang et al. (2015). The OI 557.7 nm filter has a central wavelength of 557.81 nm with a full-width half maximum of 1.53 nm. The images with the OI 557.7 filter were obtained continuously at intervals of 5 minute with an exposure time of 90-150 seconds and a spatial resolution of 500 km radial region. The OI-630.0 nm filter was not used in this period of observation.

A very-high frequency (VHF) meteor radar system has been operating at Gyeryong station (36.2°N, 127.1°E), since November, 2017. The Enhanced Meteor Detection Radar (EMDR) system (supplied by ATRAD Pty Ltd.) is an interferometric radar consisting of five channels. The system is operated with specifications of a transmitter peak power of 24 kW, duty cycle of 8.4 % from 2017/11-2018/05 and 4.2 % from 2018/05 to the present. The meteor radar provides meridional and zonal winds at 2 km bin in the 80 – 100 km altitude range every hour. The wind data were utilized when the intrinsic wave parameters and vertical propagation were examined. In addition, the temperature data between 80 and 100 km was adopted from the Sounding of the Atmosphere using Broadband Emission Radiometry (SABER) instrument (Russell et al., 1999; Mlynczak et al., 2020) onboard the TIMED satellite. The temperature measurement by SABER covers the altitude range of 15-110 km. The temperature data are selected for an airglow observation at BHO site by allowing the differences of $\pm30°$ longitudes and $\pm°8$ latitudes within 1-2 local time hours. The temperature data is utilized when the Brunt-Väisälä frequency was computed to evaluate the vertical wavelengths of gravity waves. In addition, seasonal variations of nighttime winds are identified in the middle atmosphere to confirm the filtering effect of gravity waves by using MERRA, version 2 (MERRA-2) data. MERRA-2 is an atmospheric reanalysis model created by NASA's Global Modeling and Assimilation Office (GMAO, https://gmao.gsfc.nasa.gov/reanalysis/MERRA-2/data_access/). MERRA-2 reanalysis data are available for 0-80 km altitudes and 0.5°×0.625° latitude and longitude resolutions.

## 3 Data processing for acquiring wave parameters

The procedure to acquire the wave parameters can be separated into two steps: pre-processing of all-sky camera images and the image processing with 2D image. The pre-processing includes image selection of clear nights (see Fig. 1a), star removing, transforming fisheye lens image into the horizontal plane image (500 km×500 km, see Fig. 1b) at the OI 557.7 airglow altitude of 96 km. The details of pre-processing method are provided in Kam (2016).

Time series of pre-processed images were first converted into time-difference images (Fig. 2a), from which large-scale modulation was removed by applying 2D bandpass filtering (Fig. 2b). The time-difference (TD) image is obtained from two consecutive images (see Fig. 1b) by subtracting from one to another. We then applied 2D Fast Fourier Transformation (FFT) to derive wave parameters of quasi-monochromatic waves from the series of TD images (Tang et al, 2005).

The 2D FFT operation of two TD images produces 2D spectrum arrays of $J_1$ and $J_2$, which can be cross-correlated as in Eq. (1) to derive a phase difference $(\phi_1 - \phi_2)$ of the wave

$$f(k_x, k_y) = J_1(k_x, k_y) J_2^*(k_x, k_y) = R_1 R_2 \exp(i(\phi_1 - \phi_2)), \tag{1}$$

where $k_x$ and $k_y$ are zonal and meridional wave numbers, respectively. The value of $|R_1 R_2|^2$ derived from $\left|f(k_x, k_y)\right|^2$ represents the magnitude of the wave. The dominant wave was chosen at the maximum magnitude, whose $k_x$ and $k_y$ provide the wavelengths of the dominant wave. Along with the time difference and the wavelength information, the phase difference allows to determine the observed (apparent) phase speed of the dominant wave.

## 4 Characteristics of observed waves at Mt. Bohyun

The total of 150 wave events were identified from the all-sky image data for 3 years (2017-2019). For these wave events, observed parameters of the dominant wave including horizontal wavelength, phase speed, period, and propagation direction are derived and their distributions are plotted as in Fig. 3. The interquartile range (IQR) of wavelength is spanned from 20.5-35.5 km with a median value of 27.8 km; the observed phase speed IQR is from 27.4-45.0 m/s with a median of 36.3 m/s, and the observed period IQR is from 10.8-13.7 with a median of 11.7 min. In addition, the predominant propagating directions are north (44%) and northeast (33%). The characteristics of these wave parameters were similar to the results of Kim et al. (2010).

In order to compare consistently with the results of Takeo et al. (2017), which reported the similar observation in the east Asia, we divided seasons in the same way: from February 21 - April 19 (2 months) for spring, from April 20 - August 20 (4 months) for summer, from August 21-October 20 (2 months) for fall, and from October 21 - February 20 (4 months) for winter. Seasonal wave propagation vectors and their occurrences are shown in Figs. 4a-d. The seasonal occurrences for observed (yellow) horizontal wavelength, observed phase speed, and observed period, and intrinsic (green) phase speed and

125   period are shown in Fig. 5. The mean and median values of the parameters for each season are summarized in Table 1. In spring, the propagation primarily to the northeast and next the north takes up 35% and 24% out of 29 cases, respectively, as shown in Fig. 4a. In summer, propagation directions to the north (50%) and northeast (35%) are dominant (Fig. 4b). In fall, the wave seems to propagate all-direction without preference (Fig. 4c). The fall season contains particularly small number of wave events due to equipment problem and poor weather. In winter, the propagation directions seem to be grouped into the

130   south (27%), north-westward (23%) and southwest (16%) (see Fig. 4d). In terms of the median values, the observed phase speed in winter is particularly slower than other seasons, whereas other parameters show little variation. Overall it is evident that in spring/summer, the northward and north-eastward propagating gravity waves are dominant, whereas in winter the southward and north-westward propagations are dominant. The distinct seasonal properties of propagation direction can be attributed to the filtering effect by the background wind field during the gravity wave propagation from the lower

135   atmosphere (e.g. Kim et al., 2010; Kim and Chun, 2010; Heale and Snively, 2015).

In order to confirm the filtering effect on the seasonal variation of observed propagation direction, we checked the horizontal winds of MERRA-2 data. In Figure 6 seasonal variations of night-time winds are plotted from 20-80 km (56-0.01 hPa) for 2017-2019. Here in the spring/summer the westward wind is dominant in the middle atmosphere (40-80 km), whereas in the fall/winter the eastward wind is dominant. One needs to note that the spring division (February 21 - April 19) includes some

140   of eastward wind occurrences. In addition, MR-observed annual variations of zonal and meridional winds for years of 2017-2020 are available for 80-100 km (Kam et al., 2021). Here, prevailing winds in spring and summer are observed in westward and southward at 80-100 km, seemingly continued from ~30-80 km altitudes, while in winter eastward winds are maintained in 80-100 km, but small northward winds (<~10 m/s) less than 90 km turn to the southward above 90 km. It is reasonable to suggest that westward waves in spring and summer may have been filtered out by the westward wind, and thus are hardly

145   observed. The southward wind in spring/summer may also have filtered out the southward waves, which is consistent with our observation. Furthermore, in summer it is well known that the convective system of typhoons or tropical cyclones can be significant sources of gravity waves in the middle latitude. The typhoon-generated gravity waves in the south of the Korean peninsula can propagate in any directions, but the westward propagating waves might be filtered out in the stratosphere by the prevalent westward wind. Therefore, northward or north-eastward propagating waves are obviously observed in Korea.

150   The details about typhoon-generated gravity waves can be referred to Kim and Chun (2010). In winter, it is expected that eastward/northward waves be well filtered out by prevailing the eastward/northward winds. However, although our observation shows southward/westward preferential directions (see Fig. 4d), north-westward waves are also subdominant. The significant northward component of the wave direction may not be blocked by filtering effect. In the meanwhile, it seems to survive on upward propagation up to 96 km due to the small velocity (<10 m/s) of northward mean field. Otherwise,

155   the north-westward wave in winter may be interpreted as secondary waves or waves generated in the upper mesosphere.

Previous studies of mid-latitude gravity waves have reported that gravity waves in eastward and northward propagations dominate most of the summer (Taylor et al., 1993; Nakamura et al., 1999; Walterscheid et al., 1999; Hecht et al., 2001; Ejiri et al., 2003; Tang et al., 2005). Observations at BHO have confirmed the similar tendency of propagation in summer

(Kim et al, 2010; Yang et al, 2015). The summer bias of wave propagation can be distinctly due to the critical level
filtering by the prevailing zonal and meridional winds in the lower atmosphere. However, the tendency of wave
propagation also likely shows different patterns according to localized sources. For example, in spring for Shigaraki
(34.9°N, 136.1°E) Takeo et al. (2017) observed using the OI 557.7 nm filter the dominant south-westward propagation in
addition to the north-eastward that is similar to our results in Fig. 4a. In winter, the southward (equatorward) propagation
was dominant in several studies although less than in summer (Hecht et al., 2001; Ejiri et al., 2003; Tang et al., 2005).
Both Ejiri et al. (2003) and Takeo et al. (2017) observed southward dominant propagation for Shigaraki in winter. Besides,
Ejiri et al. (2003) found that winter preferential propagation may vary with latitudes because both southward and poleward
dominant propagations in both OH and OI observations were observed at Rikubetsu (43.6°N), a relatively high latitude
site.

## 5 Characteristics of intrinsic gravity wave parameters

The OI 557.7 nm airglow layer has been reported to be peaked at 96 km with a thickness of ~7-9 km, including both
disturbed and undisturbed conditions (Vargas et al., 2007). The waves with a vertical wavelength less than the airglow layer
thickness may not be detected by an airglow imager due to sinusoidal cancellation (Nielsen et al., 2012; Vargas et al., 2007).
The vertical wavelength of the observed wave can be derived from the simplified dispersion relation of gravity waves with
excluding wind curve and wind shear terms (e.g., Nappo, 2002), such as

$$m^2 \approx \frac{N^2}{c_i^2} - \frac{1}{4H_s^2} - k^2, \tag{2}$$

where N is the Brunt-Väisälä frequency, $c_i$ is the intrinsic phase speed of gravity wave, and $H_s$ is the scale height. The MR-
measured wind profiles are not accurate enough to estimate the wind curve and shear terms. The intrinsic phase speed, $c_i$,
can be expressed as c-u, where c is the wave phase speed and u is the background wind speed in the wave propagating
direction. The Brunt-Väisälä frequency is given as

$$N^2 = \frac{g}{T}\left(\frac{dT}{dz} + \frac{g}{C_p}\right), \tag{3}$$

where $g$ is the gravity, 9.55 $m/s^2$, T is the atmospheric temperature, $C_p$ is a specific heat capacity at constant pressure,
adopted as 1005 J/(K·Kg) for a dry air (Brasseur and Solomon, 2005). $H_s$ is given with RT/g, where R is the gas constant of
dry air, 287 J/kg/K.

The intrinsic phase speeds of waves were computed by utilizing the wind at 96 km simultaneously measured by the
Gyeryong meteor radar. The intrinsic period ($\tau_i$) is calculated by $\lambda_h/c_i$, where $\lambda_h$ is the observed horizontal wavelength. The
IQR of intrinsic phase speed of gravity waves in spring is spanned from 19.4-72.0 m/s with a median value of 41.5 m/s, and
the IQR of intrinsic period is from 6.3- 20.0 min with a median of 10.0 min. In summer the corresponding IQR values are
28.2-64.0 m/s with a median of 48.1 m/s, and 6.5 – 20.9 min with a median of 9.8 min; in winter, the IQR values are 10.0 –

190     56.7 m/s with a median of 28.6 m/s, and 7.9 – 18.1 min with a median of 13.1 min. It is noted that the intrinsic speeds for spring and summer are larger than the observed ones (see Fig. 5), implying that the majority of waves occurred in the opposite direction to the background wind. The intrinsic speed has been merely shifted to the larger observed by the Doppler effect. The results of intrinsic parameters exist in the typical values of gravity wave parameters such as intrinsic phase speeds of 30-100 m/s and intrinsic periods from 5-50 min (Taylor et al., 1997; Swenson et al., 2000; Hecht et al., 2001; Ejiri et al.,

195     2003).

## 6 Characteristics of vertical propagation

The nature of vertical propagation can be evaluated by the vertical wave number squared, $m^2$ (Isler et al., 1997). If $m^2$ is greater than zero in the airglow-observed MLT region, the gravity wave is in freely propagating mode. If $m^2$ is less than zero,

200     the wave is vertically evanescent, which indicates the wave motion only in the horizontal propagation. If the freely propagating region is bounded by evanescent regions below and above, the wave is in ducting mode. If it is bounded by one side evanescent region below or above, it is in partial ducting.

    Based on the $m^2$ profile in 90-100 km centered at 96 km, the nature of vertical propagation can be classified for seasons, as summarized in Table 2. For fall season there are only a few of data available, so it is not meaningful in a statistical aspect.

205     Freely propagating waves take up a maximum of 89% in summer and a minimum of 60% in spring. For the other maximum and minimum seasons, ducted waves were 12% and 0% in spring and summer, respectively; partial ducting takes up 16% and 3% for spring and winter, respectively; evanescent waves take up 18% and 4% for winter and summer, respectively. Freely propagating waves take up a majority, while (partially) ducted waves and evanescent waves cannot be ignored. Freely propagating waves show vertical wavelengths with a median value of 14 km and IQR ranged from 6.6-19.6 km.

210     The wave ducting can be primarily caused by the background wind, so called Doppler ducting, or primarily by a variation of Brunt-Väisälä frequency, so called thermal ducting. Doppler ducting is favourable when the wind profile has a local maximum against the wave propagation, and thermal ducting is typically present at temperature increase to give a peak of $N^2$ profile (e.g., Chimonas and Hines, 1986; Isler, 1997; and Nappo, 2002; Walterscheid and Hickey, 2009). We determine Doppler ducting or thermal ducting by utilizing simultaneously measured wind profile derived from meteor radar and

215     SABER temperature in Eq.(2).

Examples of vertical propagation nature appraised by $m^2$ are shown in Figs 7a-c, where the left panel presents the $m^2$ profile, and the middle panel displays the MR wind profile projected on the wave propagating direction and the temperature (red, referring to upper thick) obtained from SABER, in which the negative wind means that the wind blows opposite to the wave propagation direction, and the right panel presents $N^2$ (red) and $\omega^2$ profiles ($\omega_i = \frac{2\pi}{\tau_i}$, where $\tau_i$ is intrinsic period).

220 In Fig. 7a the gravity wave at a phase speed of c = 82.1 m/s was propagating south-eastward ($\varphi$=135°) against the background wind at 90-100 km altitudes and the values of $m^2$ in the 90-100 km region are all positive, indicating the freely propagating nature. It might be attributed to the wave velocity far exceeding the background wind velocity (about $-30$ m/s). Figure 7b presents an example of an evanescent wave, based on negative values of $m^2$ in the altitude range of 84- 97 km. The background wind is too fast ($\sim-70$ m/s) in the opposing direction of the wave at a velocity of 17.2 m/s, prohibiting the

225 vertical propagation. Observed horizontal period is 11.8 min, while the intrinsic period is 3.2 min. The intrinsic frequency is greater than Brunt- Väisälä frequency which is typical for the atmospheric layer of evanescent wave occurring. The evanescent waves (e.g., Nielsen et al., 2012; Isler et al., 1997) may be formed by the wave upward propagating from the lower atmosphere, or by the secondary wave generated in situ at the airglow layer (e.g., Simkhada et al., 2009). Simkhada et al. (2009) presented a numerical result that evanescence occurs at 75-97 km from the wave forced below by the tropospheric

230 source. It was diagnosed that the evanescent wave might be caused by encountering the opposing strong background wind field, generating a few m/s vertical wind to cause the perturbation at airglow layer.

Figure 7c shows an example of ducting wave with a phase speed of 28.3 m/s in propagation to the north-westward. Here the freely propagating region ($m^2> 0$) at 87-96 km is encompassed with the negative values of $m^2$ above 96 km and below 81 km. The winds opposing the gravity wave propagation become large both above 96 km and lower 81 km. Here the negative

235 values of $m^2$ occurring at 96-98 km and at ~80-81 km can be attributed to the fast background winds. Therefore, the wave can be trapped around 93 km vertically, but still propagate to the horizontal direction. Nielsen et al. (2012) noted that when jets occurred above and below the altitude region of freely propagating ($m^2 > 0$), the wave can be bounded by evanescent regions ($m^2 < 0$), causing Doppler ducting. Suzuki et al. (2013) observed an evidence of Doppler ducting under the large opposing winds: a northward propagating wave at a phase speed of 48 m/s lasting for ~5 hrs (11-17 UT) went through a

240 strong southward wind, stretching over 16°x16° in latitude and longitude. The ducted wave can be identified as Doppler ducting, associated with fast winds.

Figure 7d shows an example of partial ducting, above which an evanescent region is formed. For such a partial ducting, in the upper part an evanescent region ($m^2<0$) seems to be related to $N^2$ decreasing and a peak of freely propagating ($m^2>0$) at 94 km corresponds to a peak of $N^2$. According to this, the evanescent wave appears closely associated with a variation of $N^2$,

245 identified with thermal ducting.

In Table 3, the ducted and partially ducted waves are categorized into either Doppler or thermal ducting. Here, it can be seen that the wave ducting above Korean Peninsular occur with almost equal probability of Doppler ducting or thermal ducting, although the number of observed ducting cases is not sufficient to indicate local trend.

250

**7 Summary and conclusions**

This study investigated the characteristics of horizontal and vertical propagation of atmospheric gravity waves observed at Mt. Bohyun observatory (BHO, 36.2°N, 128.9°E) for the period of 2017 - 2019. The data used are all-sky images of the OI 557.7 nm airglow layer (~96 km). Wind data in the 80 -100 km altitude range measured by a meteor radar at a nearly co-located site were utilized to derive intrinsic wave parameters and their vertical propagation nature.

The results of our analysis can be summarized as follows:

1) The total of 150 wave events were identified in the images of 144 clear nights. The interquartile ranges (IQR) of wavelength, observed phase speed, and observed periods of the identified waves are 20.5 - 35.5 km (with a median value of 27.8 km), 27.4 - 45.0 m/s (with a median value of 36.3 m/s) and 10.8 -13.7 min (with 11.7 min median value), respectively.

2) The observed waves propagate predominantly north-eastward and northward in spring and summer, respectively. In winter the majority of waves propagate southward but the significant portion of waves northward. The seasonal preferential directions as in our observation have been reported by previous studies in east Asia, and interpreted as the consequence of the critical level filtering effect due to the prevailing wind in the lower atmosphere. The observed north-westward waves in winter may be caused by nullified filtering effect due to small background wind field, secondary waves or waves generated in the upper mesosphere.

3) Intrinsic phase speeds and periods of the waves were also derived by using both the wind data simultaneously observed by a meteor radar and temperature data observed by TIMED/SABER. It is noted that the intrinsic speeds for spring and summer are larger than the observed ones because the majority of waves propagate in the opposite direction to the background wind.

4) The nature of vertical propagation was evaluated in each season. The freely propagating waves take up a maximum of 89% in summer and a minimum of 60% in spring. For other maximum and minimum seasons, ducted waves were 12% and 0% in spring and summer, respectively. Evanescent waves were 18% and 4% in winter and summer, respectively. The majority of observed waves are found to be freely propagating. The ducted wave is more favourable in spring and the evanescent wave is more favourable in winter.

In conclusion, we find that both horizontal and vertical propagation characteristics of the observed waves at the OI 557.7 nm airglow layer are consistent with the notion that the majority of waves originated from the lower atmosphere and experienced the filtering effect by the prevailing winds in the intermediate atmosphere.

**Data availability**. We referred free reanalysis wind data from https://goldsmr5.gesdisc.eosdis.nasa.gov/data/MERRA2
/M2T3NVASM.5.12.4/, last access on November 20, 2020, for the seasonal night-time mean wind field at altitudes of 20-80
km. We also used TIMED/SABER data from ftp site saber.gats-inc.com, last access on July 20, 2021 as an element in
making our figures and table.

**Supplement**. Not applicable.

**Author Contributions.** Y. H. Kim and Y.-S. Lee conceived of the presented idea and the design of the study. J.-Y. Hwang
and Y.-S. Lee manually gathered the data used. J.-Y. Hwang, S.M. Song and Y.-S. Lee programmed for data analysis. The
data analysis and interpretation of the results were done by Y. H. Kim and Y.-S. Lee. This paper was drafted and edited by
Y.-S Lee and J.-Y. Hwang, and critically reviewed by T.-Y. Yang, H. Kam, Y.-S. Kwak and Y. H. Kim for content. Y.-S.
Kwak and T.-Y. Yang took responsibility for overseeing the project. All authors have read and agreed to the published
version of the manuscript.

**Competing interests**. The contact author has declared that neither they nor their co-authors have any competing interests.

**Disclaimer**. Publisher's note: Copernicus Publications remains neutral with regard to jurisdictional claims in published maps
and institutional affiliations.

**Acknowledgements.**
This research was supported by basic research funding from the Korea Astronomy and Space Science Institute (KASI)
(KASI2021185005). We would like to thank the anonymous reviewers for the critical reviews that helped to improve this
paper.

**Review statement**. This paper was edited by an editor and reviewed by two anonymous referees.

# References

Brasseur, G., and Solomon, S.: Aeronomy of the Middle Atmosphere: Chemistry and Physics of the Stratosphere and Mesosphere (3rd ed.). Dordrecht: Springer, 2005.

Becker, E.: Dynamical control of the middle atmosphere. Space Sci. Rev., 168(1-4), 238-314, doi:10.1007/s11214-011-9841-5, 2012.

Chimonas, G., and Hines, C. O.: Doppler ducting of atmospheric gravity waves, J. Geophys. Res., 91, 1219–1230, 1986.

Ejiri, M., Shiokawa, K., Ogawa, T., Igarashi, L., Nakamura, T., and Tsuda, T.: Statistical study of short-period gravity waves in OH and OI nightglow images at two separated sites, J. Geophys. Res., 108(D21), 4679, doi:10.1029/2002JD002795, 2003.

Fritts, D. C., and Vincent, R.A.: Mesospheric momentum flux studies at Adelaide, Australia: Observations and a gravity wave/tidal interaction model, J. Atmos. Sci., 44, 605–619, 1987.

Fritts, D. C., and Alexander, M.J.: Gravity wave dynamics and effects in the middle atmosphere. Rev. Geophys., 41(1), 1-68, doi:10.1029/2001RG000106, 2003.

Gelaro, R., McCarty, W., Suárez, M. J., Todling, R., Molod, A., Takacs, L., and Wargan,K.: The modern-era retrospective analysis for research and applications, version 2 (MERRA-2). J. Climate, 30(14), 5419-5454, 2017.

Heale, C. J., and Snively, J.B.: Gravity wave propagation through a vertically and  horizontally inhomogeneous background wind, J. Geophys. Res. Atmos., 120, 5931–5950, doi:10.1002/ 2015JD023505, 2015.

Hecht, J. H., Walterscheid, R.L., Hickey, M., and Franke, S.: Climatology and modelling of quasi-monochromatic atmospheric gravity waves observed over Urbana, Illinois, J. Geophys. Res., 106(D6), 5181–5196, 2001.

Isler, J. R., Taylor, M.J., and Fritts, D.C.: Observational evidence of wave ducting and evanescence in the mesosphere, J. Geophys. Res., 102, 26,301–26,313, 1997.

Kam, H. (2016), Analysis of mesospheric gravity waves observed by an All-sky airglow camera at King Sejong Station, Antarctica, Master's thesis, Chungnam National University.

Kam, H., Kwak, Y.-S., Yang, T.-Y., Kim, Y., Kim, J., Lee, J., Choi, S., Baek, J.-H.: J. Astron. Space Sci 38(4), 229-236. https://doi.org/10.5140/JASS.2021.38.4.229, 2021.

Kim, S-Y. and Chun, H. Y.: Stratospheric Gravity Waves Generated by Typhoon Saomai (2006): Numerical Modeling in a Moving Frame Following the Typhoon, J. Atmos. Sci., 67, 3617-3636, 2010.

Kim, Y. H., Lee, C. S., Chung, J. K., Kim, J. H., and Chun, H. Y.: Seasonal variations of mesospheric gravity waves observed with an airglow all-sky camera at Mt. Bohyun, Korea (36 N). J. Astron. Space Sci., 27(3), 181-188, 2010.

Lindzen, R. S.: Turbulence and stress owing to gravity wave and tidal breakdown. J. Geophys. Res. Oceans., 86(C10), 9707-9714, doi:10. 1029/JC086iC10p09707, 1981.

Mlynczak, M. G., Daniels, T., Hunt, L. A., Yue, J., Marshall, B. T., Russell, J. M., Remsberg, E. E., Tansock, J., Esplin, R., Jensen, M., Shumway, A., Gordley, L., and Yee, J. H.: Radiometric Stability of the SABER Instrument, Earth Space Sci.,

350    7(2), 1–8, https://doi.org/10.1029/ 2019EA001011, 2020.

Nakamura, T., Higashikawa, A., Tsuda, T., and Matsushita, Y.: Seasonal variations of gravity wave structures in OH airglow with a CCD imager at Shigaraki. Earth, planets and space, 51(7-8), 897-906, 1999.

Nappo, C.J.: An Introduction to Atmospheric Gravity Waves. Academic Press, San Diego, 2002.

Nielsen, K., Taylor, M. J., Hibbins, R.E., Jarvis, M.J. and Russell III, J.M.: On the nature of short-period mesospheric
355    gravity wave propagation over Halley, Antarctica, J. Geophys. Res., 117, D05124, doi:10.1029/2011JD016261, 2012.

Pautet, P., Taylor, M.J., Liu, A.Z., and Swenson, G.R.: Climatology of shot-period gravity waves observed over Northern Australia during the Darwin Area Wave Experiment (DAWEX) and their dominant source regions, J. Geophys. Res., 110, D03S90, doi:10.1029/2004JD004954, 2005.

Russell III, J. M., Mlynczak, M. G., Gordley, L. L., Tansock, Jr., J. J., and Esplin, R. W.: Overview of the SABER
360    experiment and preliminary calibration results, Proc. SPIE, 3756, 277-288, https://doi.org/10.1117/12.366382, 1999.

Simkhada, D.B., Snively, J.B., Taylor, M.J., and Franke, S.J.: Analysis and modelling of ducted and evanescent gravity waves observed in the Hawaiian airglow, Ann. Geophys., 27, 3213-3224, 2009.

Suzuki, S., Shiokawa, K., Otsuka, Y., Kawamura, S., and Murayama, Y.: Evidence of gravity wave ducting in the mesopause region from airglow network observations, Geophys. Res. Lett., 40, 601–605, doi:10.1029/2012GL054605, 2013.

365    Swenson, G. R., Alexander, M. J., and Haque, R.: Dispersion imposed limits on atmospheric gravity waves in the mesosphere: Observations form OH airglow, Geophys. Res. Lett., 27(6), 875–878, 2000.

Takeo, D., Shiokawa, K., Fujinami, H., Otsuka, Y., Matsuda, T. S., Ejiri, M. K., and Yamamoto, M.: Sixteen year variation of horizontal phase velocity and propagation direction of mesospheric and thermospheric waves in airglow images at Shigaraki, Japan. J. Geophys. Res.: Space Physics, 122(8), 8770-8780, 2017.

370    Tang, J., Kamalabadi, F., Franke, S. J., Liu, A. Z. and Swenson, G. R.: Estimation of gravity wave momentum flux with spectroscopic imaging. IEEE transactions on geoscience and remote sensing, 43(1), 103, 2005.

Taylor, M. J., Ryan, E. H., Tuan, T. F., and Edwards, R.: Evidence of preferential directions for gravity wave propagation due to wind filtering in the middle atmosphere. J. Geophys. Res. Atm., 98, 6047-6057. http://doi.org/10.1029/92JA02604, 1993.

375    Taylor, M. J., Pendleton Jr., W.R., Clark, S., Takahashi, H., Gobbi, D., and Goldberg, R.S.: Image measurements of short-period gravity waves at equatorial latitudes, J. Geophys. Res., 102, 26,283, 1997.

Vargas, F., Swenson, G., Liu, A., and Gobbi, D.: O(1S), OH, and O2(b) airglow layer perturbations due to AGWs and their implied effects on the atmosphere, J. Geophys. Res., 112, D14102, doi:10.1029/2006JD007642, 2007.

380

Walterscheid, R., Hecht, J., Vincent, R., Reid, I., Woithe, J., and Hickey, M.: Analysis and interpretation of airglow and radar observations of quasi-monochromatic gravity waves in the upper mesosphere and lower thermosphere over Adelaide, Australia (35°S, 138°E), J. Atmos. Sol. Terr. Phys., 61(6), 461–478, doi:10.1016/S1364-6826(99)00002-4, 1999.

385 Walterscheid, R. L., and Hickey, M. P.: Gravity Wave Ducting in the Upper Mesosphere and Lower Thermosphere Duct System. Journal of Geophysical Research: Atmospheres, 114(D19). https://doi.org/10.1029/2008JD011269, 2009.

Yang, T.Y., Kwak, Y.-S., Kim, Y.H.: Statistical comparison of gravity wave characteristics obtained from airglow all-sky observation at Mt. Bohyun, Korea and Shigaraki, Japan, J. Astron. Space Sci., 32(4), 327-333, 2015.

390

420
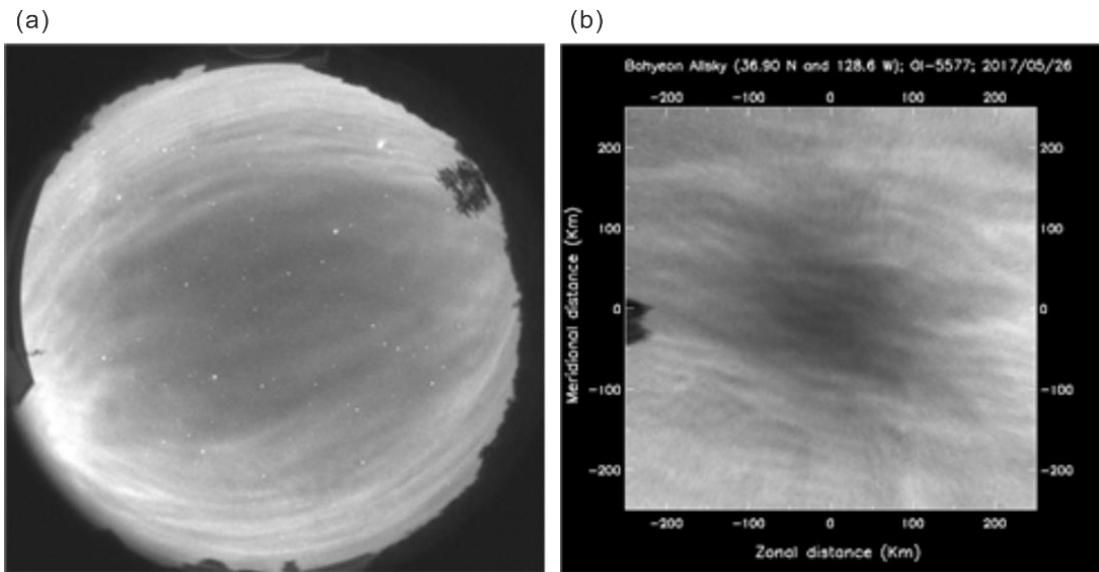
Figure 1: (a) an all-sky image with the OI 557.7 nm filter and (b) an image after star removal and coordinate transformation. The image was observed at 15:32:33 UT on May 26,2017.
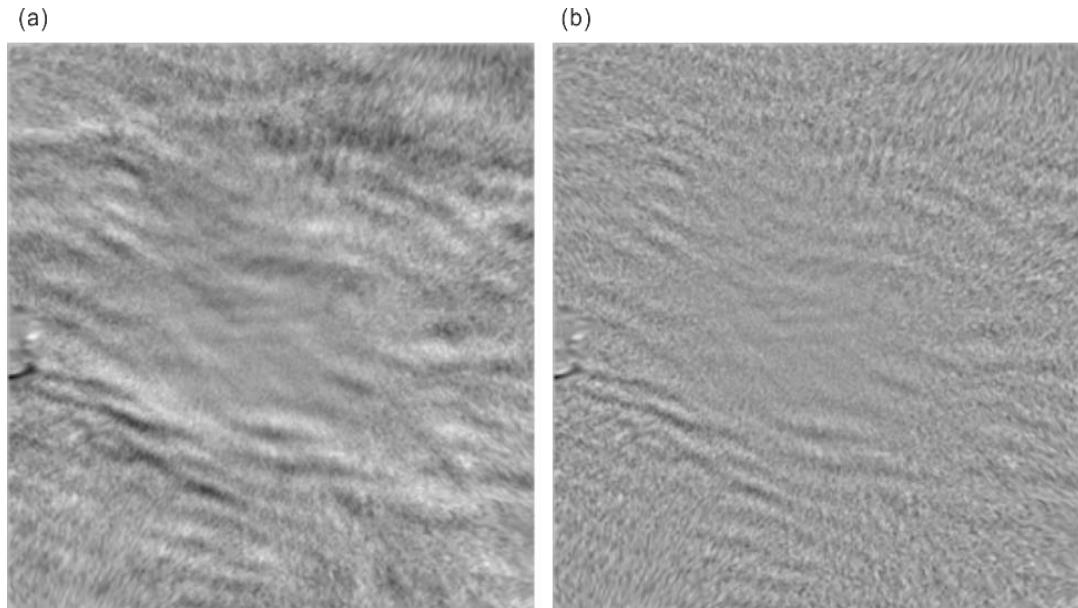
425    Figure 2: (a) A time-difference image (TD image) obtained by taking a subtraction between two successive images, (b) an image after large-scale modulation removed from (a) by applying 2-D bandpass filtering.
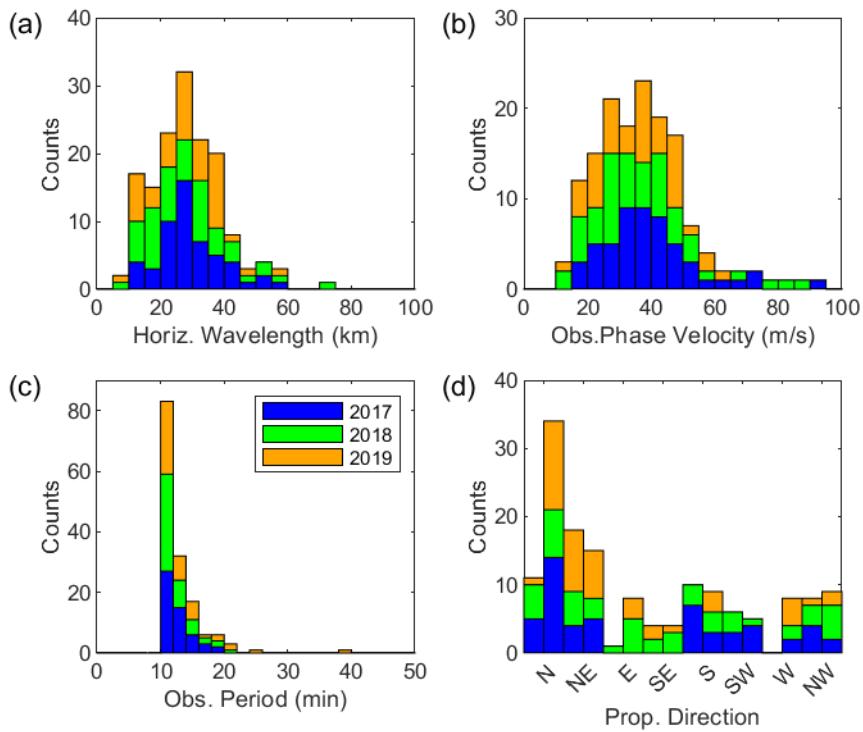
430

Figure 3: The parameters of the observed waves in the OI 557.7 airglow layer from 2017-2019, (a) wavelength, (b) phase velocity, (c) period, and (d) propagation direction. Colours of blue, green, and orange correspond to each year of 2017-1019, respectively.

435

440
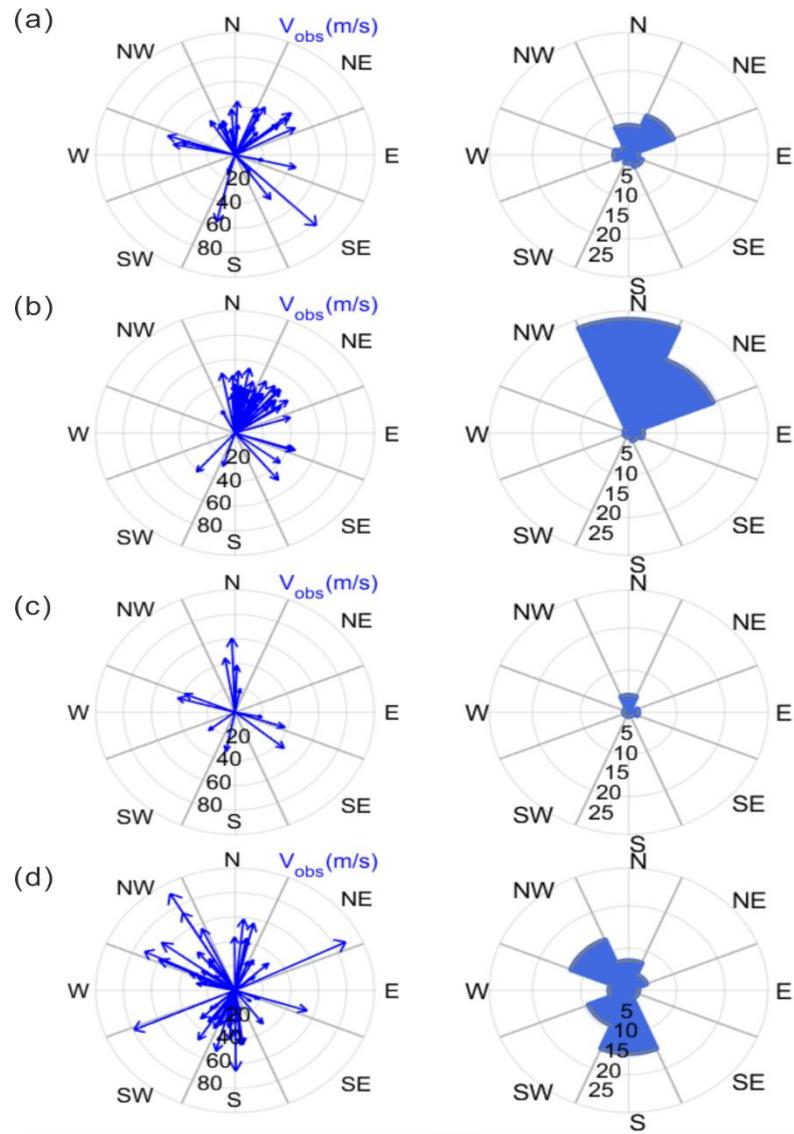
Figures 4: Propagation vectors (left) and the occurrences (right) of observed waves in the OI airglow over the three years from 2017 to 2019. (a) Spring, (b) Summer, (c) Fall and (d) Winter. The number on the arc lines indicate (left) the phase velocity and (right) occurrences in each radial direction. Wave propagation directions are divided into eight regions by a clockwise azimuth angle of 45° from -22.5° to 315°, corresponding to the north (N), northeast (NE), east (E), southeast (SE), etc. In fall, both equipment problem and poor weather resulted in particularly the small number of observations comparing to other seasons.
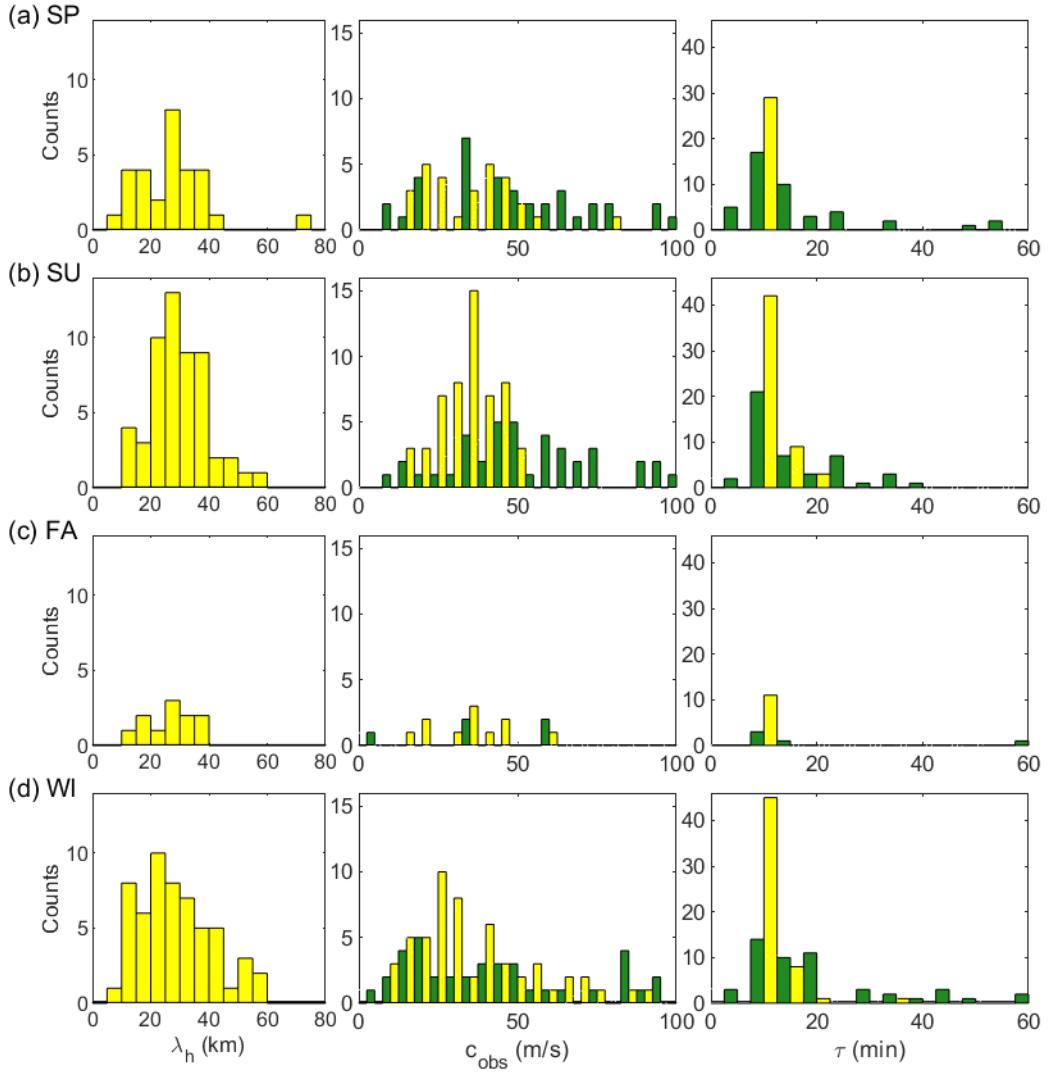
Figure 5: Seasonal distributions of observed (yellow) and intrinsic (green) wave parameters. Each row represents (a) Spring, (b) Summer, (c) Fall, and (d) Winter. Observed gravity waves are in total 150 events from April, 2017 to December, 2019, while intrinsic wave parameters were derived for 95 events when both wind data and temperature data were available from the nearly co-located meteor radar and a nearby area overpassed by TIMED/SABER, respectively.
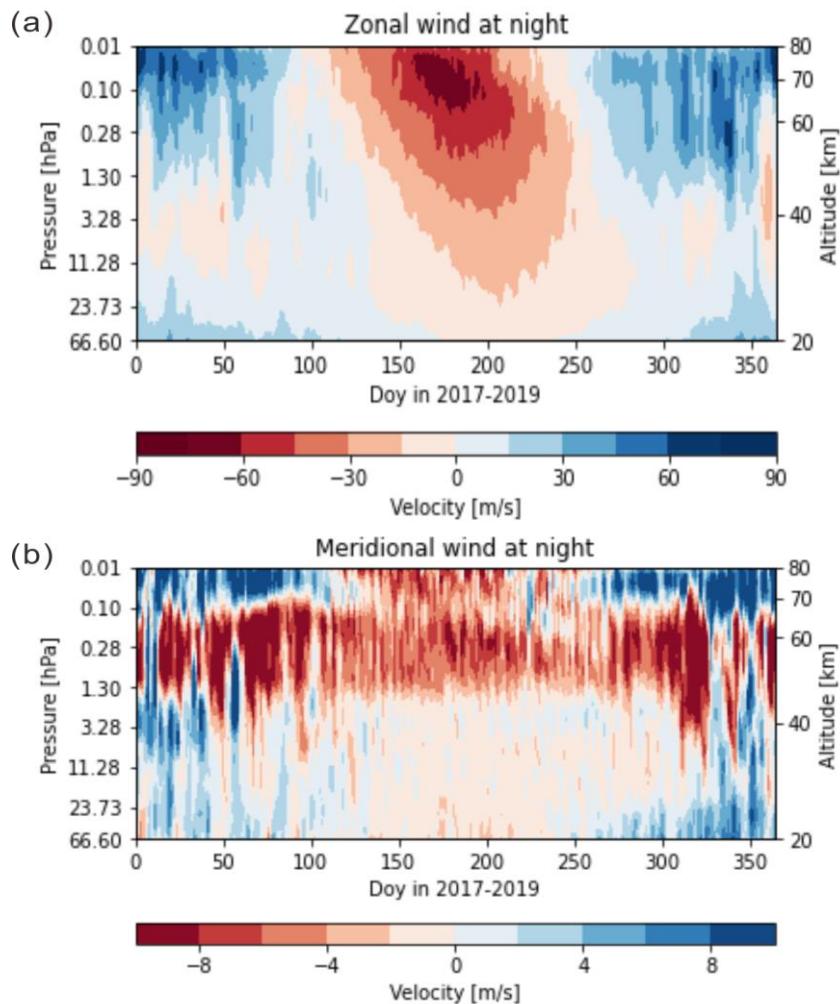
Figure 6: Seasonal variations of night-time (upper) zonal and (lower) meridional wind vectors in terms of day number (1-356) and 20-80 km (56-0.01 hPa) altitude from MERRA-2 reanalysis data for 2017-2019.
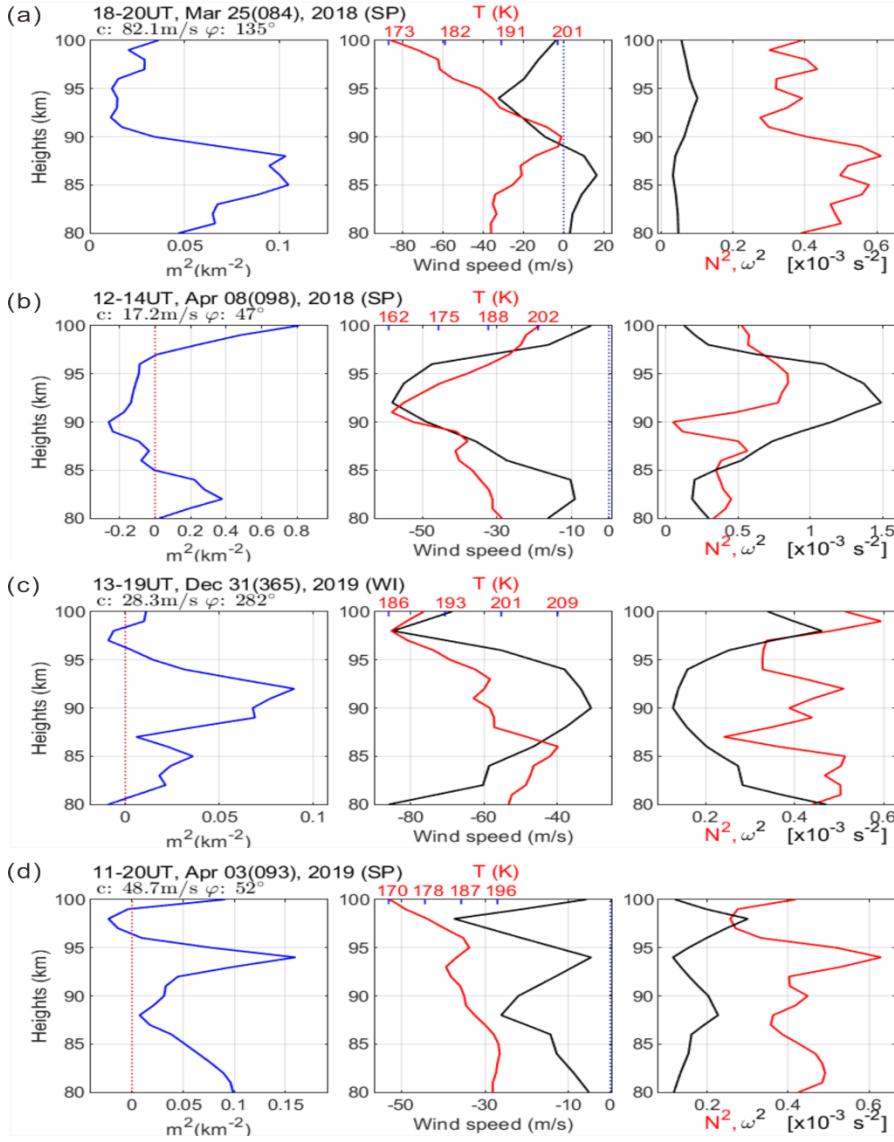
Figure 7: Examples of vertical propagation characteristics evaluated by vertical wave number squared, $m^2$, and the relation with temperature and horizontal wind. (left) the profile of $m^2$; (middle) Wind speed aligned to wave propagating direction and Temperature (red); (right) Brunt-Väisälä frequency squared ($N^2$, red) and intrinsic frequency squared ($\omega^2$). (a) freely propagating, (b) evanescent based on negative $m^2$ at 90-97 km, (c) Ducted as encompassed by negative $m^2$, and (d) Partially ducted by above $m^2$. Each title noted with the applied gravity wave occurring time, date and season. In addition, c and $\varphi$ indicate the apparent phase speed and azimuth angle of the horizontal propagation, respectively.

Table 1: Seasonal median values and interquartile ranges (IQR) of observed wave parameters (horizontal wavelength ($\lambda$), phase speed ($c_{obs}$) and period ($\tau$)) observed at Mt. Bohyun for 2017-2019.

| Seasons | Parameters | $\lambda_{obs}$ (km) | $c_{obs}$ (m/s) | $\tau_{obs}$ (min) |
|---|---|---|---|---|
| Spring | Mean | 27.2±12.5 | 36.9±14.7 | 12.1± 1.3 |
| | Median | 26.2 | 38.0 | 11.8 |
| | IQR | 18.0-31.4 | 24.8- 45.2 | 10.9- 13.6 |
| Summer | Mean | 29.5±9.6 | 36.5±9.0 | 13.5±3.0 |
| | Median | 29.0 | 37.1 | 12.5 |
| | IQR | 23.7- 36.1 | 30.5- 42.1 | 11.3- 14.4 |
| Fall | Mean | 26.1±8.8 | 37.1±12.3 | 11.7±1.0 |
| | Median | 25.7 | 38.7 | 11.7 |
| | IQR | 18.1-34.4 | 24.2- 45.1 | 10.7- 12.6 |
| Winter | Mean | 28.6±12.5 | 37.8±20.3 | 13.0±4.4 |
| | Median | 27.5 | 32.7 | 11.5 |
| | IQR | 19.4-35.8 | 25.1- 46.7 | 10.8- 14.2 |

485

Table 2: Vertical propagation nature of gravity waves at Mt. Bohyun for 2017-2019.

| | Spring (%) | Summer (%) | Fall (%) | Winter (%) |
|---|---|---|---|---|
| Freely Propagating | 60 | 89 | 0 | 69 |
| Ducting | 12 | 0 | 50 | 10 |
| Partial Ducting | 16 | 7 | 50 | 3 |
| Evanescent | 12 | 4 | 0 | 18 |
| Total (no. events) | 25 | 27 | 4 | 39 |

490

Table 3: Classification of ducted and partially ducted waves into thermal or Doppler ducting.

| | Ducting event no. (9) | Partial ducting events no. (9) |
|---|---|---|
| Doppler ducting | 5 | 5 |
| Thermal ducting | 4 | 4 |